AGU PUBLICATIONS

JGR

Journal of Geophysical Research: Atmospheres

RESEARCH ARTICLE
10.1002/2015JD024304

Key Points:
- Cirrus cloud thinning intensifies precipitation and evaporation
- Cirrus cloud thinning cools Earth's climate with amplified Arctic cooling
- Effective radiative forcing is nonlinear with ice particle fall speed change

Supporting Information:
- Supporting Information S1

Correspondence to:
L. S. Jackson,
l.s.jackson@leeds.ac.uk

Citation:
Jackson, L. S., J. A. Crook, and P. M. Forster (2016), An intensified hydrological cycle in the simulation of geoengineering by cirrus cloud thinning using ice crystal fall speed changes, *J. Geophys. Res. Atmos.*, *121*, 6822–6840, doi:10.1002/2015JD024304.

Received 3 OCT 2015
Accepted 21 MAY 2016
Accepted article online 27 MAY 2016
Published online 23 JUN 2016

An intensified hydrological cycle in the simulation of geoengineering by cirrus cloud thinning using ice crystal fall speed changes

L. S. Jackson[1], J. A. Crook[1], and P. M. Forster[1]

[1]Institute for Climate and Atmospheric Science, School of Earth and Environment, Maths/Earth and Environment Building, University of Leeds, Leeds, UK

Abstract Proposals to geoengineer Earth's climate by cirrus cloud thinning (CCT) potentially offer advantages over solar radiation management schemes: amplified cooling of the Arctic and smaller perturbations to global mean precipitation in particular. Using an idealized climate model implementation of CCT in which ice particle fall speeds were increased 2×, 4×, and 8× we examine the relationships between effective radiative forcing (ERF) at the top of atmosphere, near-surface temperature, and the response of the hydrological cycle. ERF was nonlinear with fall speed change and driven by the trade-off between opposing positive shortwave and negative longwave radiative forcings. ERF was $-2.0\,\mathrm{Wm}^{-2}$ for both 4× and 8× fall speeds. Global mean temperature decreased linearly with ERF, while Arctic temperature reductions were amplified compared with the global mean change. The change in global mean precipitation involved a rapid adjustment (~ 1%/Wm^2), which was linear with the change in the net atmospheric energy balance, and a feedback response (~2%/°C). Global mean precipitation and evaporation increased strongly in the first year of CCT. Intensification of the hydrological cycle was promoted by intensification of the vertical overturning circulation of the atmosphere, changes in boundary layer climate favorable for evaporation, and increased energy available at the surface for evaporation (from increased net shortwave radiation and reduced subsurface storage of heat). Such intensification of the hydrological cycle is a significant side effect to the cooling of climate by CCT. Any accompanying negative cirrus cloud feedback response would implicitly increase the costs and complexity of CCT deployment.

1. Introduction

Geoengineering Earth's climate by intentional reduction of cirrus cloud coverage and optical thickness, referred to here as cirrus cloud thinning (CCT), has been suggested as a way to moderate climate change due to increased greenhouse gas concentrations [*Mitchell and Finnegan*, 2009]. The mean radiative forcing at the top of atmosphere (TOA) for cirrus clouds is estimated to be $-51\,\mathrm{Wm}^{-2}$ for shortwave (SW) radiation and $+55\,\mathrm{Wm}^{-2}$ for longwave (LW) radiation [*Hong and Liu*, 2015], resulting in a net warming of Earth's climate.

Climate model simulations have shown that CCT could potentially cool Earth's climate. *Storelvmo et al.* [2013] used a cirrus cloud scheme adapted to enable explicit treatment of ice cloud formation conditions, ice nuclei properties, and competition between homogeneous and heterogeneous ice nucleation. They found that net cloud radiative forcing (CRF) became more negative with cirrus cloud seeding, although the magnitude of CRF varied nonlinearly with ice nuclei concentration. The maximum reduction in CRF was $2\,\mathrm{Wm}^{-2}$. CRF increased to a positive forcing for the largest increases in ice nuclei concentration. CRF comprised an increase in outgoing longwave radiation (OLR) at the TOA, which was amplified by reductions in upper tropospheric water vapor and was partly offset by an increase in net incoming SW radiation at the TOA. Consequently, globally nonuniform seeding strategies, e.g., minimal seeding in the summer hemisphere, could potentially reduce CRF by more than $2\,\mathrm{Wm}^{-2}$ [*Storelvmo and Herger*, 2014].

In a simulation using a coupled atmosphere-ocean general circulation model (GCM), CCT cooled Earth's climate by 1.4°C [*Storelvmo et al.*, 2014]. Climate model simulations of the climate response to CCT, in which CCT was approximated by an increase in ice particle fall speed (fall speed was doubled by *Muri et al.* [2014] and quadrupled by *Crook et al.* [2015]), yielded reductions in CRF and cooling of global annual mean temperature (−0.94°C and −1.0°C, respectively).

CCT potentially offers the advantage of reduced side effects from geoengineering compared to solar radiation management (SRM) [*Storelvmo and Herger*, 2014]. SRM reduced global mean precipitation in climate model simulations that offset a greenhouse gas-induced increase in temperature [*Bala et al*., 2008]. The reduction in precipitation is robust across different climate models [*Tilmes et al*., 2013] and different SRM methods [*Niemeier et al*., 2013]. *Bala et al.* [2008], *Tilmes et al.* [2013], and *Niemeier et al.* [2013] all found that the reduction in net SW radiation flux at Earth's surface from SRM was associated with reduced surface evaporation and weakening of the hydrological cycle. In simulations of CCT, however, global mean precipitation changes were small [*Muri et al*., 2014] or involved relatively small reductions [*Storelvmo et al*., 2014]. In a comparison of CCT and SRM methods using the same climate model and identical simulation design, *Crook et al.* [2015] found that CCT increased global precipitation in contrast to decreases found for all of the SRM methods tested. *Kristjánsson et al.* [2015] also found that precipitation was significantly enhanced by CCT.

Globally uniform forcing from SRM is a poor match to the zonal pattern of warming from increased concentrations of greenhouse gases; the tropics are cooled too much and the Arctic too little [*Kravitz et al*., 2013a]. In simulations of CCT, the Arctic was cooled more strongly than global mean temperatures [*Muri et al*., 2014; *Storelvmo et al*., 2014; *Crook et al*., 2015]. CCT potentially provides a better fit to the zonal pattern of anthropogenic warming than SRM methods.

CCT involves large-scale manipulation of the Earth's radiation fluxes [*Boucher et al*., 2014] and, crucially, a trade-off between opposing forcings of similar magnitude (cooling from increased OLR and warming from increased incoming SW radiation). This trade-off is illustrated by the sensitivity of cirrus cloud CRF at the TOA which changes from positive to negative net forcing at greater optical depths [*Corti and Peter*, 2009; *Hong and Liu*, 2015].

In this study, we address the following question: How does precipitation respond to different changes in ice particle fall speed and which physical processes support any increase in global mean precipitation? We also investigate whether effective radiative forcing (ERF) [*Myhre et al*., 2013] changes linearly with the scale of CCT, and what are the relationships between changes in global mean cloud cover, global temperature, Arctic temperature, and precipitation?

Using a simplified climate model simulation design, we approximated the cirrus cloud effects of CCT by increases in ice particle fall speeds of 2×, 4×, and 8×, leaving ice particle effective diameter and the shape of the ice particle size distribution unchanged. We use the same climate model and simulation design as *Crook et al.* [2015] and begin our analysis by comparing the responses of global mean cloud cover, temperature, and precipitation to CCT (section 3.1). We quantify ERF at the TOA for the three CCT simulations (section 3.2) and describe changes in ice particle concentration and cloud cover. Next, we describe the changes in water vapor and humidity (section 3.4), temperature (section 3.5), and precipitation (section 3.6). Changes in TOA energy fluxes and meridional heat transport are analyzed to investigate the mechanisms underlying the sensitivity of the temperature response (section 3.5). Changes in precipitation minus evaporation ($P - E$) and soil moisture are analyzed to give a broader perspective on the sensitivity of the hydrological cycle (section 3.7). Finally, to understand the physical mechanisms underlying changes in precipitation and evaporation, we analyze changes in atmospheric vertical motion, moisture divergence, the boundary layer climate, and surface energy fluxes (section 3.8).

We do not consider engineering aspects of CCT or its economic viability. We do not consider risks to the environment from injection of seeding material into the atmosphere which could be washed into the marine and terrestrial environments. Finally, while social and ethical issues raised by the prospect of geoengineering are of great importance [e.g., *Corner and Pidgeon*, 2014], they are also beyond the scope of this study.

2. Climate Model, Data, and Methods

2.1. Climate Model

Hadley Centre Global Environment Model version 2 (HadGEM2) [*Martin et al*., 2011; *Hardiman et al*., 2012], a coupled atmosphere-ocean GCM, was used for the simulations. The Earth system components of HadGEM2 were diagnostic with the carbon cycle feedback turned off. The model did, however, include the effects of altered transpiration by stomatal resistance.

The model atmosphere had 60 vertical levels extending to 84.5 km altitude, which provided enhanced representation of stratospheric dynamics and radiation and incorporated parameterization of stratosphere-troposphere aerosol gravitational sedimentation. The model atmosphere had a horizontal resolution of 1.25° latitude by 1.875° longitude. The model ocean had 40 vertical levels and a horizontal resolution of 1° latitude between the poles and 30°N/S increasing smoothly to 0.333° at the equator and a 1° longitude resolution. A time step of 20 min was used for the atmosphere, 60 min for the ocean, and exchanges between the atmosphere and ocean models were updated daily.

The land surface scheme within HadGEM2 was the Met Office Surface Exchanges Scheme II [*Cox et al*., 1999; *Essery et al*., 2003]. This scheme included parameterization of soil moisture in four layers, each with its own soil temperature and moisture content.

Cloud microphysical processes were based on the scheme of *Wilson and Ballard* [1999] (HadGEM2 microphysics scheme 3C). The scheme was configured with standard HadGEM tunings for the ice particle size distribution parameters and for the ice particle mass-diameter relationship. Microphysical processes involving ice included nucleation, gravitational sedimentation, deposition of cloud liquid water and water vapor, aggregation, riming, melting, and sublimation. Homogeneous nucleation of liquid water occurred at temperatures less than −40°C with all liquid water instantly frozen to form ice particles [*Rogers and Yau*, 1989]. Heterogeneous nucleation was active when three conditions were fulfilled: temperatures were less than −10°C; the total mass of active nuclei produced each time step was less than the total mass of active nuclei that would be produced according to the temperature-dependent relationship of *Fletcher* [1962], which is also described in *Wilson and Ballard* [1999]; and the vapor pressure exceeded a temperature-dependent threshold [*Heymsfield and Miloshevich*, 1995]. Ice particles were divided between two modes, large mode and small mode, and each mode had its own particle size distribution, mass-diameter relation, and fall-speed diameter relationship [*Mitchell*, 1996].

2.2. Simulation Design

We simulated the climate of the 21st century from 2020 to 2069. The simulations were started from 1 January 2020 using an initial climate state spun-up with natural and anthropogenic forcings for the period of 1860–2005 and Representative Concentration Pathway 4.5 (RCP4.5) [*Moss et al*., 2010] for 2006–2019. Greenhouse gas and aerosol concentrations for 2020–2069 were based on RCP4.5, in which radiative forcing at the TOA is projected to increase to 4.5 Wm^{-2} by 2099. This represents a possible scenario in which CCT might be deployed along with some climate change mitigation. The control simulation was RCP4.5 with no geoengineering.

We assume that CCT works as proposed by *Mitchell and Finnegan* [2009] and that the cirrus cloud microphysical processes affected by CCT are approximated sufficiently well by an increase in ice particle fall speed as described by *Muri et al.* [2014]. Injecting cirrus cloud formation regions with efficient ice nuclei (e.g., bismuth triiodide) could potentially reduce cirrus cloud coverage and optical thickness [*Mitchell and Finnegan*, 2009]. The presence of efficient ice nuclei is expected to promote the heterogeneous nucleation of ice particles, e.g., as described in *Cziczo et al.* [2013], in very cold cirrus cloud-forming regions in which homogeneous nucleation normally prevails. Heterogeneous nucleation, in regions that have ice nuclei concentrations within an optimal range [*Storelvmo et al*., 2013], would lead to the growth of larger ice crystals which have greater fall speeds. This would lower cirrus cloud lifetime and optical depth and transport water vapor to warmer ambient air temperatures increasing OLR. This cooling effect would be opposed by a reduction in cirrus cloud solar albedo.

Three geoengineering simulations were run, each identical to RCP4.5 except for geoengineering by CCT of constant magnitude implemented by a uniform scaling of ice particle fall speed. A geoengineering simulation in which ice particle fall speed increased 2× (GEO2) was run to facilitate comparison with *Muri et al.* [2014]. Simulations with ice particle fall speed increased 4× and 8× (GEO4 and GEO8, respectively) were run to investigate the sensitivity of forcing and climate response to different magnitudes of CCT. Large increases in fall speed were used to amplify forcing and climate response signals relative to the model climate internal variability. Increases in fall speed for GEO4 and GEO8 are unlikely to be realistic except for ice particles with relatively small diameters because the fall speed/particle diameter relationship is square root in shape [e.g., *Mitchell*, 1996]. The realism of the 2× fall speed increase also remains uncertain and warrants further evaluation in climate models with more explicit treatment of seeding and ice nucleation. To illustrate the uncertainties, we refer to the finding of *Storelvmo and Herger* [2014], in which optimal seeding was

achieved with an increase in ice particle effective radius (R_e) of ~5 μm which is an increase of 20% if we assume a mean R_e of 25 μm at 200 hPa [e.g., see *Storelvmo and Herger*, 2014, Figure 2]. *Muri et al.* [2014] showed regional-scale increases in R_e of ~5 μm with 2× fall speed. In contrast, the ice fall speed/effective diameter (D_e) relationships of *Mishra et al.* [2014] suggest that increases in D_e of 40%–50% would be required to double ice fall speeds.

The increase in fall speed was applied globally and throughout the calendar year to both small- and large-mode ice particles. It was applied only in atmospheric levels where air temperature was colder than −40°C, and ice crystal fall speed was assumed to slow abruptly on subsequent falling through the −40°C isotherm. CCT started in full from 2020 and ended abruptly after 2069 to match the Geoengineering Model Intercomparison Project (GeoMIP) G4 scenario [*Kravitz et al.*, 2011]. One climate model realization was produced for each simulation.

2.3. Analysis of Results

ERF was used to measure the radiative forcing of CCT. ERF is the change in radiative fluxes at the TOA allowing for changes in atmospheric temperature, water vapor, and clouds but without changes in surface temperatures [*Myhre et al.*, 2013]. ERF was estimated using the method of *Gregory et al.* [2004]. Global annual mean TOA radiative flux anomalies, determined using differences between the CCT simulations and RCP4.5 for the period of 2020–2029, were regressed on global annual mean near-surface temperature anomalies. A 10 year period was used because the temperature reduction driven by CCT largely occurred within 10 years. Over longer periods of time, temperature changes were more strongly influenced by internal variability and the emergent climate system response to the transient forcing of RCP4.5. The intercept of the regression line was interpreted as the ERF and the standard error of the intercept as a measure of uncertainty in this ERF estimate. Correlation coefficients from the calculation of ERF, data for the forcings, and the associated standard errors are shown in Table S1 in the supporting information.

Rapid adjustments, sometimes described as the fast response [*Andrews et al.*, 2010], were estimated using linear regression based on the method of *Gregory and Webb* [2008]. Global annual mean anomalies (e.g., for precipitation), determined using differences between the CCT simulations and RCP4.5 for the period of 2020–2069 and expressed as percentage changes, were regressed on global annual mean near-surface temperature anomalies (°C). The intercept of the regression line was interpreted as the estimated rapid adjustment and the slope the estimated climate feedback (slow response).

To assess the impact of CCT on climate, CCT simulations were compared with RCP4.5 using time series data from 2020 to 2069 and 40 year means for 2030–2069. The 2030–2069 period was chosen because global mean temperature responses to CCT had ceased cooling compared with RCP4.5 by 2030 and for consistency with GeoMIP G4 simulations [*Kravitz et al.*, 2011]. A 40 year period was used for climate means to strengthen the geoengineering signal over internal climate variability compared to shorter-period means. As only one climate model realization was produced for each simulation, we have focused on global and large-scale changes in climate.

Meridional energy transport was calculated by integrating the zonal mean net energy balance starting from the South Pole and progressing northward, a method widely used with both climate model outputs and observations [e.g., *Frierson et al.*, 2013]. Total atmospheric and ocean heat transport was inferred from integration of the TOA radiation balance. Ocean heat transport was inferred from integration of the surface energy balance, and atmospheric heat transport was determined as the residual after ocean transport was subtracted from total heat transport.

Tests of statistical significance were performed using a two-tailed Student's *t* test at the 5% significance level. Degrees of freedom were adjusted to account for autocorrelation in time series data [*Zwiers and von Storch*, 1995].

3. Results

3.1. Introduction

There were contrasting responses in global mean climate to CCT. Cloud cover decreased and the changes were greater with greater fall speeds (Figure 1a). Global mean near-surface temperature decreased (Figure 1b), but the changes were nonlinear with the fall speed change. Arctic temperature changes were amplified compared to global mean temperature changes and were greater with accelerated fall speed

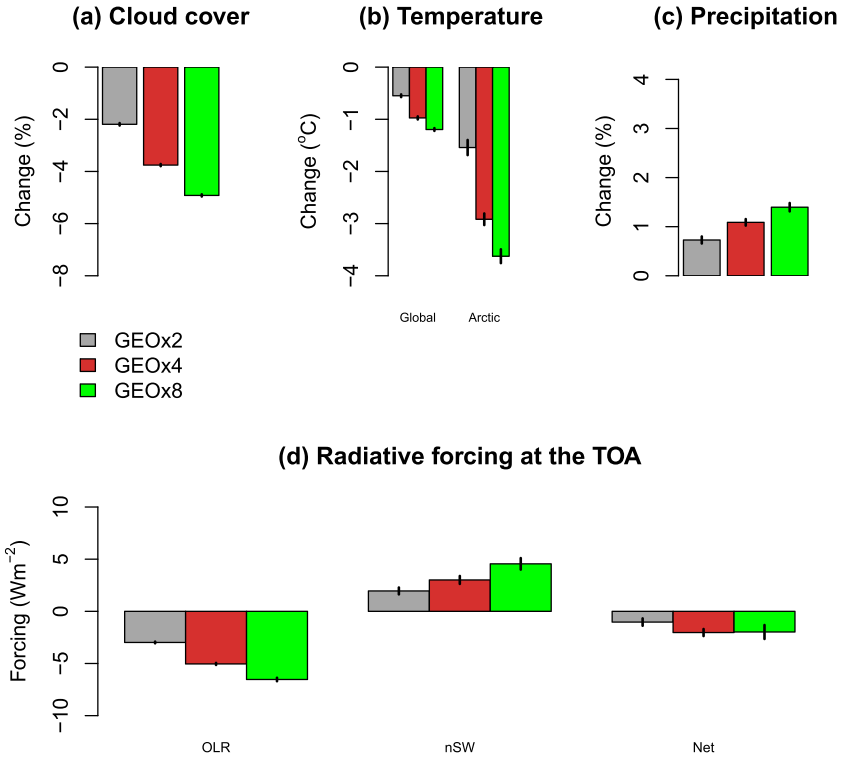

Figure 1. (a–c) Change in 2030–2069 global annual mean for CCT geoengineering compared to RCP4.5. (d) CCT radiative forcing at the TOA for outgoing longwave radiation (OLR), net shortwave radiation (nSW), and net radiation (Net). The error bars (black) represent ±1 standard error.

change. In contrast to temperature changes, global mean precipitation increased with increasing fall speed change (Figure 1c) and the precipitation increase was strongly anticorrelated with the change in cloud cover (correlation coefficient −1.0).

3.2. ERF at the TOA

Global mean ERF comprised a negative LW forcing, due to reduced cirrus cloud absorption of upwelling LW radiation, opposed by a positive SW forcing due to reduced cirrus cloud reflectance of incoming SW radiation (Figure 1d). Net radiative forcing at the TOA was found to have a linear relationship with the change in global mean near-surface temperature (correlation coefficient +0.92).

The magnitude of clear-sky forcing for both LW and SW radiation (not shown) was much smaller than all-sky forcing, which indicates that cloud changes were the driving physical process. Net radiative forcing peaked at $-2.0\,\mathrm{Wm}^{-2}$ (GEO4 and GEO8). This nonlinearity in forcing with fall speed change was associated with differences between the relative sensitivities of LW and SW radiation to fall speed changes: at slower fall speeds (GEO2 and GEO4), OLR increased more strongly in response to fall speed than SW radiation; at faster fall speeds (GEO8), SW radiation was more responsive.

3.3. Ice Particle Concentration and Cloud Cover

The increase in fall speed affected ice particle concentrations throughout the troposphere, across all latitudes, and the magnitude of the changes increased with accelerated fall speeds. The fall speed change was concentrated in the upper troposphere where atmospheric temperatures were colder than −40°C and where ice particle concentrations were relatively high (Figure 2a). Ice particle concentrations decreased between 5 and 14 km altitude for GEO2, GEO4, and GEO8 and in line with the increase in fall speed. For GEO2, GEO4, and GEO8 there was an increase in ice particle concentration below 5 km height. In Figures S1–S4 in the supporting information we show latitude-longitude maps of the changes in ice water path and liquid water path and height-latitude cross sections of the changes in ice water content and liquid water content.

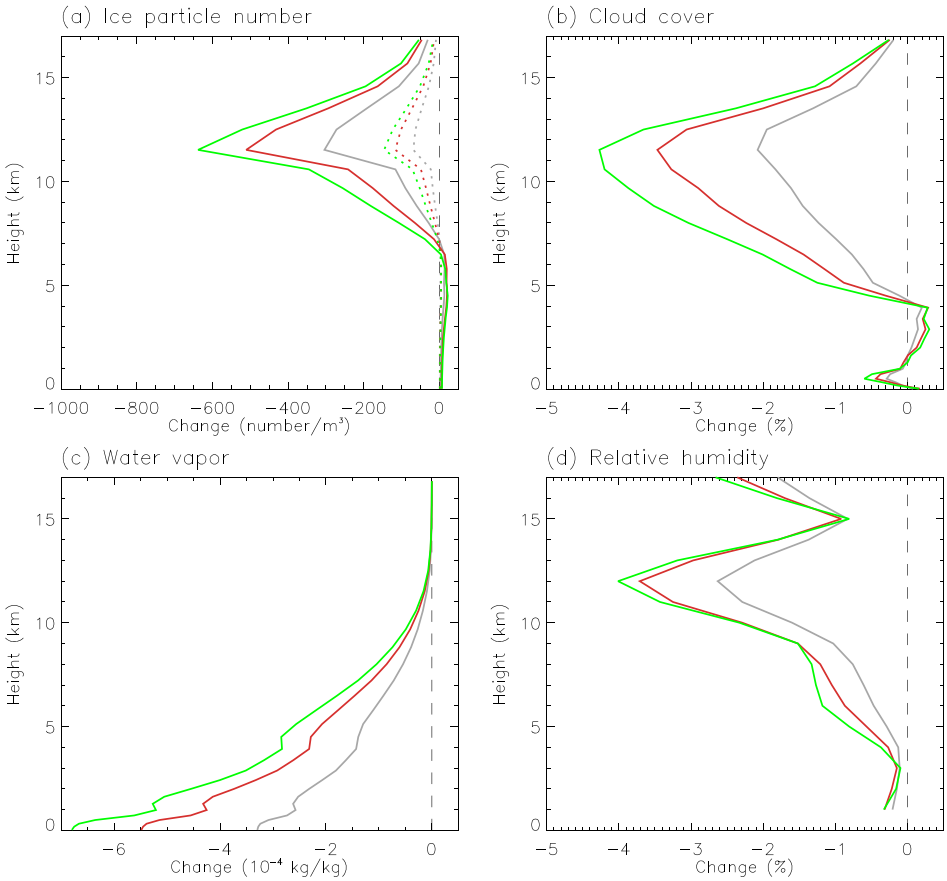

Figure 2. (a–d) Mean vertical profiles during 2030–2069 of changes in GEO2, GEO4, and GEO8 compared to RCP4.5. Color scheme: GEO2 (gray), GEO4 (brown), and GEO8 (green). In Figure 2a the changes in ice particle number concentration are shown, assuming that all ice particles were large-mode particles (solid lines) or small-mode particles (dotted lines).

Cloud cover changes emulated the changes in ice particle concentration (Figure 2b). As well as the anticipated thinning of cirrus cloud, there was some increase in low/middle-level cloud cover. This increase was a cloud feedback response to the cooling of the troposphere. This was established by linear regression of the change in low/middle-level cloud cover on the change in temperature. For GEO2, GEO4, and GEO8 the slopes of the regression lines were statistically significant and the intercept terms were not significantly different from zero. For GEO2, GEO4, and GEO8 the geographic distribution of the increase in low/middle-level cloud cover was strongly coupled with changes in the atmospheric water budget: in 85% of the regions where low/middle-level cloud cover increased, precipitation or surface evaporation also increased.

The decrease in cloud cover in the lowest 1 km of the atmosphere was concentrated in the extratropical and polar regions (south of 50°S and north of 60°N). The decrease occurred as a cloud feedback response to the CCT and, within the polar regions, is likely a positive feedback that amplified the regional cooling.

Column-integrated cloud cover changes occurred as rapid adjustments (reductions) triggered by the fall speed increases (Figures 3a and 3b), which increased in magnitude in line with the fall speed change.

3.4. Total Column Water Vapor and Relative Humidity

Total column water vapor (TCWV) responded differently to ice particle concentration and cloud cover to the increased fall speed: its changes were principally driven by a feedback response related to temperature change.

Water vapor decreased throughout the atmospheric column with the greatest changes in the lower to middle tropical troposphere, reflecting the tropospheric distribution of water vapor (Figure 2c). Relative humidity decreased strongly at heights where ice particle concentrations decreased mostly strongly (Figure 2d). The increased ice particle fall speed accelerated the transport of water vapor to lower heights through

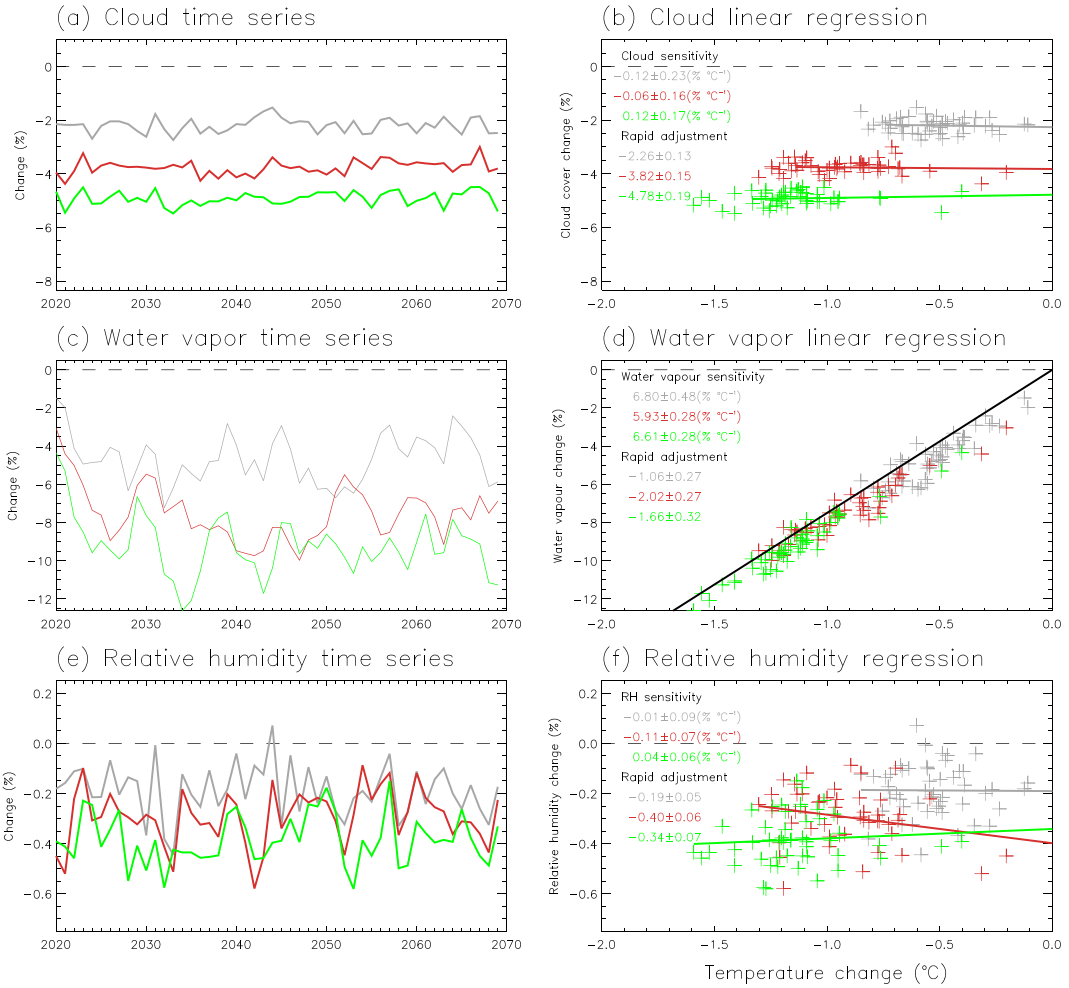

Figure 3. Annual mean time series for (a) cloud, (c) TCWV, and (e) relative humidity compared to RCP4.5. Linear regression of the change in (b) cloud cover, (d) TCWV, and (f) relative humidity on temperature change for 2020–2069. The black line in Figure 3d shows a sensitivity in TCWV of 7.5% $°C^{-1}$. Color scheme: GEO2 (gray), GEO4 (brown), and GEO8 (green).

accelerated ice particle descent. Associated changes in the vertical profile of atmospheric latent heating also promoted the change in vertical profile of relative humidity.

Global mean TCWV decreased by 5.0 ± 1.3%, 8.1 ± 1.2%, and 10.0 ± 1.3% during 2030–2069 for GEO2, GEO4, and GEO8, respectively, compared to RCP4.5. These changes were strongly correlated with ERF at the TOA (correlation coefficient +0.91) and with the change in near-surface temperature for 2030–2069 (correlation coefficient 1.00). The fall speed increase triggered rapid adjustments in TCWV (Figures 3c and 3d), which were statistically significant but small compared with the accumulated change in TCWV. The slow climate response of TCWV was 6–7% $°C^{-1}$ change in temperature, i.e., marginally less than predicted by the Clausius-Clapeyron relationship.

Surface air relative humidity (at 1.5 m) decreased by a rapid adjustment that was triggered by the fall speed increases (Figures 3e and 3f) and had a magnitude in proportion to the ERF. This decrease in relative humidity was driven by rapid dynamical changes in the atmosphere. In regions of descending air, the atmosphere was drier with decreased relative humidity. Relatively small changes in relative humidity occurred, however, in the regions of ascending air which were common to both RCP4.5 and CCT.

3.5. Temperature

Cooling of global mean near-surface air temperatures (Figure 1b) occurred within the first 10 years of starting CCT after which temperature anomalies tracked their original RCP4.5 trend (Figure 4a). The reductions in global mean temperature during 2030–2069 were 0.55 ± 0.16 °C, 0.97 ± 0.18 °C, and 1.20 ± 0.16 °C for GEO2,

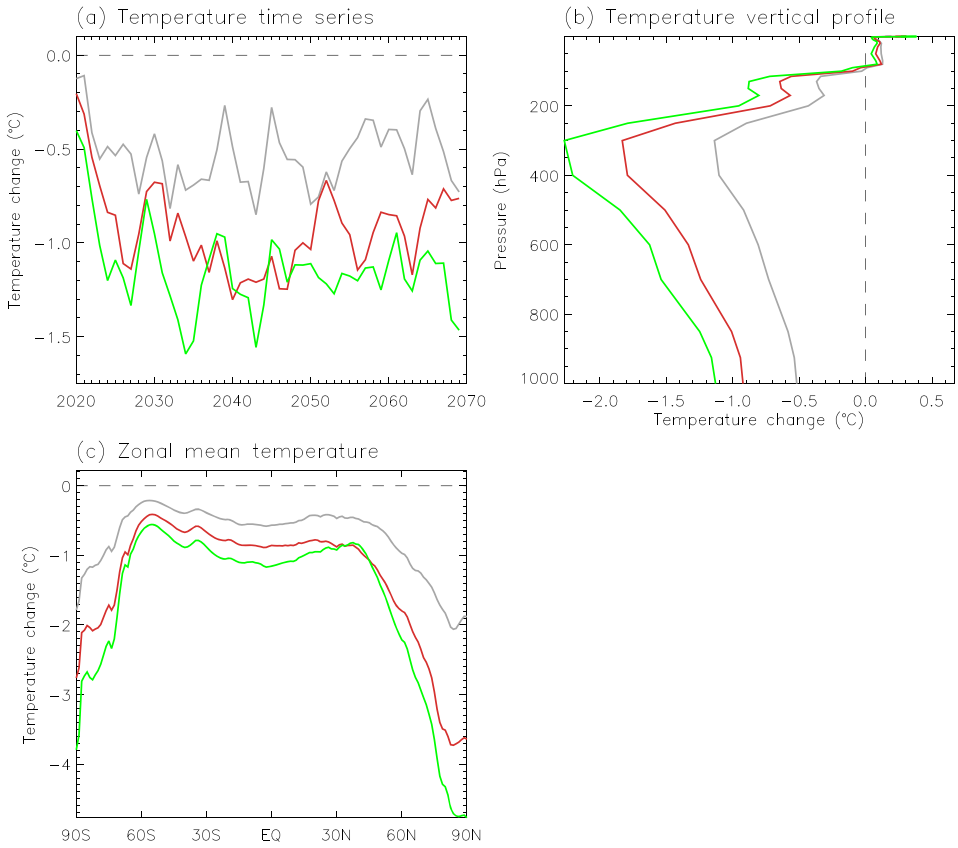

Figure 4. (a) Temperature anomaly time series compared to RCP4.5 for CCT geoengineering. (b) Change in vertical profile of 2030–2069 global annual mean temperature for CCT geoengineering compared to RCP4.5. (c) Change in 2030–2069 zonal mean temperature for CCT geoengineering compared to RCP4.5. Color scheme: GEO2 (gray), GEO4 (brown), and GEO8 (green).

GEO4, and GEO8, respectively, and reduced linearly with ERF at the TOA (correlation coefficient +0.92). The reductions in global mean temperature maintained their relationship with ERF throughout the vertical profile of the troposphere (Figure 4b). The greatest reductions occurred in the upper troposphere at the altitude of the greatest reductions in ice particle concentrations and cirrus cloud cover (Figure 2).

There was an amplified temperature response to CCT in the polar regions (Figures 1b and 4c). The potential for warming from increased downwelling SW radiation due to CCT was mitigated by the relatively low Sun angles and seasonal absence of sunshine [*Storelvmo et al*., 2014] and by the high surface albedo of snow cover and sea ice in polar regions (Figures 5a and 5b; changes in OLR are shown Figure S5). In the Arctic, there is also a positive feedback from increased sea ice cover which contributed to a net reduction in SW radiation available to the climate system at the TOA over the Arctic (Figures 5c and 5d). Over Antarctica, all-sky and clear-sky net SW radiation at the TOA (Figures 5c and 5d) changed little except at its coastal boundary, where it reduced due to an increase in sea ice area. Annual mean 2030–2069 Antarctic sea ice area increased by 4.5 ± 4.0%, 10.9 ± 4.9%, and 13.5 ± 4.4% for GEO2, GEO4, and GEO8, respectively. In the Arctic, all-sky and clear-sky net SW radiation at the TOA deceased due to expansion of sea ice and enhancement of surface albedo, as shown in the energy budget analysis of *Tilmes et al.* [2014] for geoengineering using SRM. Weaker cooling in the polar regions for GEO2 compared to the other CCT simulations was accompanied by less expansion of the sea ice area and smaller changes in the net SW radiation flux at the TOA. Annual mean 2030–2069 Arctic sea ice area increased by 10.4 ± 2.1%, 20.2 ± 1.4%, and 24.1 ± 2.2% for GEO2, GEO4, and GEO8, respectively.

Ocean meridional heat transport played a role in the amplified cooling of the Arctic region. While ocean meridional heat transport changed little south of 60°S, north of 60°S, the northward ocean heat flux weakened and most significantly in the Northern Hemisphere (NH; Figures 6a and 6b). Changes in atmospheric heat

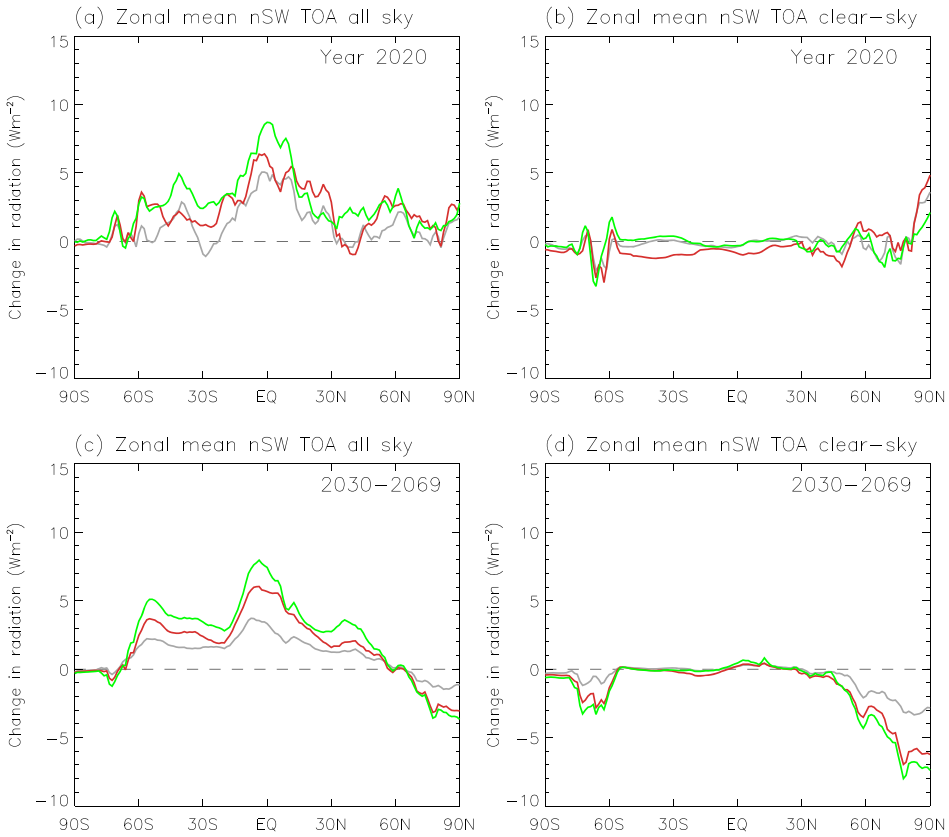

Figure 5. Change in zonal mean net SW radiation at the TOA for GEO2, GEO4, and GEO8 compared to RCP4.5: (a and c) all sky and (b and d) clear sky. Figures 5a and 5b show the anomalies for year 2020 only. Figures 5c and 5d show the anomalies for years 2030–2069. An increase in downward energy flux is represented by positive values. Color scheme: GEO2 (gray), GEO4 (brown), and GEO8 (green).

transport contributed to the amplified cooling of both polar regions. The weakening of poleward atmospheric heat fluxes was, however, relatively small poleward of 60°N and 60°S (Figures 6c and 6d).

3.6. Precipitation

The change in global mean precipitation involved a rapid adjustment on starting CCT, a weakened trend during the first 10 years of CCT, and resumption of the RCP4.5 trend thereafter (Figure 7a). The rapid adjustment to precipitation, or fast response [*Andrews et al.*, 2010], was the largest component of change in precipitation and was greater for greater fall speed increases. The increases in global mean precipitation during 2030–2069 were 0.73 ± 0.14%, 1.09 ± 0.13%, and 1.40 ± 0.17% for GEO2, GEO4, and GEO8, respectively. These increases included a feedback response which had a linear relationship with the change in temperature, the slow response [*Andrews et al.*, 2010]. The magnitude of the feedback response (Figure 7b), diagnosed using the slope of the linear regression of the precipitation change on temperature change and expressed as a hydrological sensitivity (% °C^{-1}), appears independent of the CCT ERF at ~2% °C^{-1} for all three CCT fall speed changes and is at the lower end of the range 2.0–3.3% °C^{-1} found in Coupled Model Intercomparison Project phase 5 GCMs for quadrupled CO_2 concentrations [*Mauritsen and Stevens*, 2015]. In simulations of CCT using a climate model with slab oceans, *Kristjánsson et al.* [2015] (Figure 1) found similar relationships for changes in latent heat flux and temperature: latent heat fluxes increased as a fast response to CCT, and feedback responses for changes in CO_2 concentration and CCT levels were statistically equivalent to each other.

We defined the change in the column-integrated atmospheric energy balance (ΔQ) to be given by

$$\Delta Q = \Delta R_{sfc} - \Delta R_{TOA} + \Delta_{sh} \quad (1)$$

where ΔR_{TOA} is the change in net radiation fluxes at the TOA, ΔR_{sfc} is the change in net radiation fluxes at the surface, and Δ_{sh} is the change in sensible heating of the atmosphere at the surface (following *Muller and*

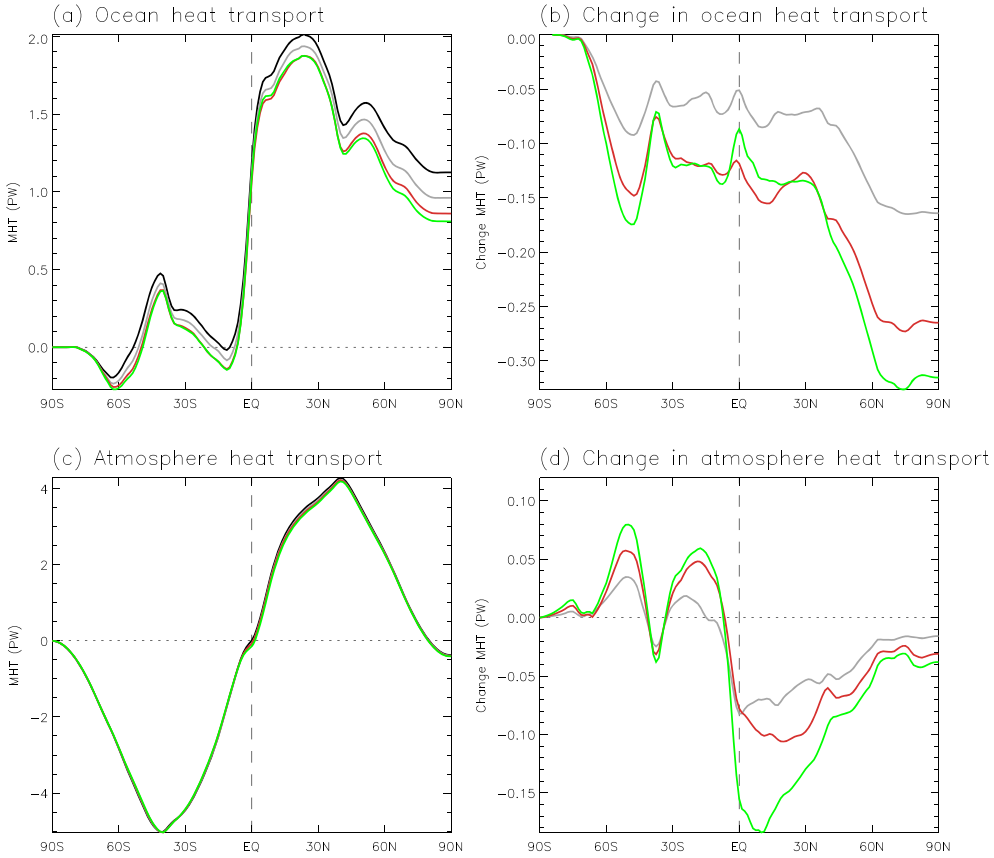

Figure 6. (a) Mean ocean heat transport during 2030–2069 for RCP4.5 and the three CCT simulations with positive values indicating a northward heat flux. (b) Changes in mean ocean heat transport during 2030–2069 for the three CCT simulations compared to RCP4.5. (c) Equivalent of Figure 6a for atmospheric heat transport. (d) Equivalent of Figure 6b for atmospheric heat transport. Color scheme: RCP4.5 (black), GEO2 (gray), GEO4 (brown), and GEO8 (green).

O'Gorman [2011] and *O'Gorman et al.* [2012]). We found that the increase in global precipitation was strongly associated with the net change in atmospheric energy balance (Figure 7c), consistent with the findings of *Mitchell et al.* [1987], *O'Gorman et al.* [2012], and *Pendergrass and Hartmann* [2014].

Figure 7c also shows that changes in the atmospheric energy budget accounted for both rapid adjustments in global annual mean precipitation and subsequent interannual changes in precipitation. All three CCT simulations displayed linear relationships with correlation coefficients stronger than −0.97 and with intercepts of zero precipitation change at zero change in the atmospheric energy balance. The sensitivities of global precipitation to changes in atmospheric energy budget were $\sim -1.0 \pm 0.1\%/\mathrm{Wm}^{-2}$ independent of the change in fall speed. When we split the radiation terms on the right-hand side of equation (1) into components for changes in atmospheric LW radiative cooling and atmospheric absorption of SW radiation, we found that changes in atmospheric LW radiative cooling dictated the relationship with precipitation: precipitation increased with an increase in LW atmospheric cooling rate. Contributions from changes in the atmospheric absorption of SW radiation and from surface sensible heating of the atmosphere were not statistically significant. Changes in the atmospheric energy balance have previously been shown to account for changes in global mean precipitation in simulations of geoengineering, e.g., in experiment G1 of GeoMIP [*Kravitz et al.*, 2013b] and for CCT [*Kristjánsson et al.*, 2015].

The zonal patterns of precipitation change were similar for the CCT simulations (Figure 7d). There was a northward shift in precipitation across the equator. The mean latitude of precipitation falling between 15° N and 15°S of the equator shifted northward by 0.3° for GEO2 and GEO4 and by 0.5° latitude for GEO8.

The northward shift in tropical precipitation occurred because of asymmetric changes in the column-integrated net energy fluxes of the atmospheres of the NH and Southern Hemisphere (SH; Figures 8a–8c).

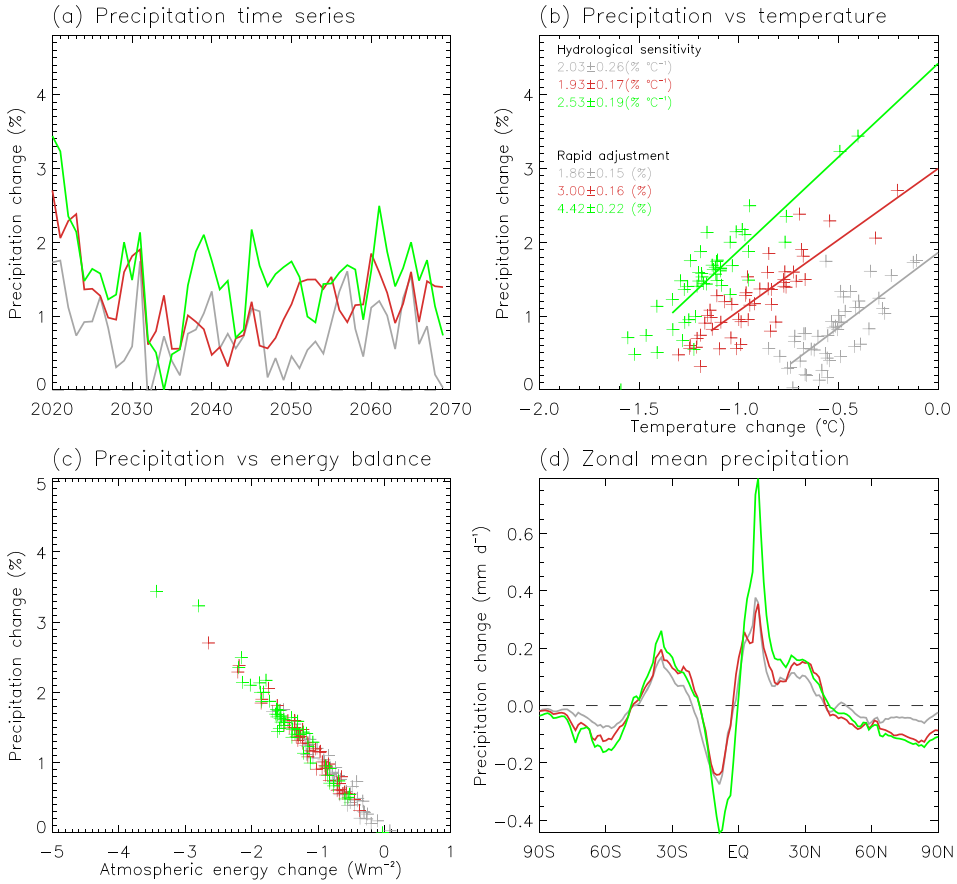

Figure 7. (a) Precipitation anomaly time series for the three CCT simulations compared to RCP4.5, (b) linear regression of the change in precipitation (%) on the change in temperature for 2020–2069, (c) change in annual global mean precipitation plotted against the change in atmospheric energy balance for 2020–2069, and (d) changes in the 2030–2069 zonal mean precipitation for the three CCT simulations compared to RCP4.5. Color scheme: GEO2 (gray), GEO4 (brown), and GEO8 (green).

The net energy flux into the NH atmosphere increased under CCT: the reduced net radiation flux at the TOA was compensated for by a weakened flux of heat into the oceans. In contrast, the net energy flux into the SH atmosphere reduced. We plotted the northward shift of annual mean precipitation between 15°N and 15°S against the hemispheric asymmetry in net atmospheric energy fluxes (Figure 8d). They were strongly correlated with correlation coefficients of 0.88, 0.86, and 0.88 for GEO2, GEO4, and GEO8, respectively. *Frierson and Hwang* [2011] identified similar relationships using an ensemble of slab ocean climate models and obtained a correlation coefficient of 0.93. The most significant changes in heat transport by the atmosphere occurred in the southward cross-equator transport of heat which strengthened for GEO2, GEO4, and GEO8 (Figure 6d). The strengthened southward Hadley cell heat fluxes in the upper troposphere were coupled with strengthened northward moisture flux in the lower troposphere (850 hPa). This is consistent with the northward shift of the ascending branch of the Hadley cell and the Intertropical Convergence Zone (ITCZ) described by *Crook et al.* [2015] for GEO4.

Asymmetric changes to energy fluxes into the atmosphere of the NH relative to the SH have previously been shown to change cross-equatorial energy transport and shift the location of the ITCZ and tropical precipitation in the opposing meridional direction [*Kang et al.*, 2008; *Yoshimori and Broccoli*, 2008]. Meridional shifts in the mean location of the ITCZ have been shown to be driven by differences in forcing between the NH and SH [*Haywood et al.*, 2013]. The roles of climate feedback and extratropical influences (e.g., changes in Arctic sea ice coverage) were demonstrated by *Frierson and Hwang* [2011].

The reduction in precipitation in the NH extratropics (Figure 7d) is strongly influenced by the thermodynamically reduced atmospheric moisture-holding capacity. In GEO2, which had a relatively small reduction in NH

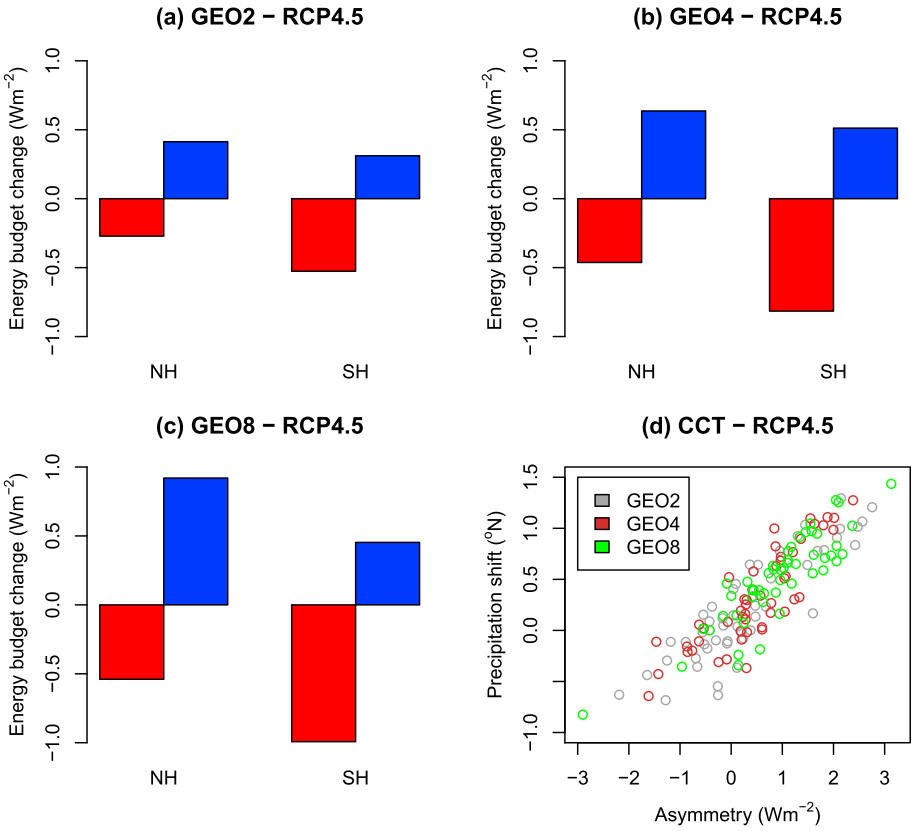

Figure 8. (a–c) Change in Northern hemisphere (NH) and Southern Hemisphere (SH) mean energy balances at the TOA and surface for 2020–2069. Positive values represent a positive energy flux toward the atmosphere. (d) Scatterplot of the northward shift in precipitation that falls between latitudes 15°S and 15°N and the asymmetry in hemispheric energy balance for the atmosphere (NH less SH). The data points show the annual mean values for each year from 2020 to 2069.

extratropical temperature (Figure 4c), there was a relatively small reduction in precipitation. In GEO4 and GEO8, in which NH extratropical temperatures decreased by ~1.5°C, the moisture-holding capacity of the atmosphere would have decreased ~10% according to the Clausius-Clapeyron relationship.

3.7. Precipitation Less Evaporation and Soil Moisture

Global mean precipitation less evaporation at the surface (P − E) decreased during 2030–2069 compared with RCP4.5 with reductions of 0.7 ± 0.2%, 1.1 ± 0.2%, and 1.4 ± 0.2% for GEO2, GEO4, and GEO8, respectively. These reductions occurred immediately after the start of CCT as a rapid adjustment, the increase in evaporation exceeding the increase in precipitation. There was no statistically significant trend in P − E (Figure 9a). The change in global P − E was strongly anticorrelated with the change in global precipitation (correlation coefficient −1.0).

Over land (excluding Greenland and Antarctica), precipitation and evaporation both increased with fall speed and P − E changed by +2.3 ± 2.2%, +1.9 ± 1.7%, and −0.5 ± 2.2% for GEO2, GEO4, and GEO8, respectively (Figure 9b). With large interannual variations in P − E over land and changes that were not statistically significant, it was not possible to determine whether CCT triggered rapid adjustments in P − E over land.

Even with the large interannual variations in P − E over land, changes in land mean soil moisture during 2030–2069 were statistically significant and increased by 1.1 ± 0.2%, 1.8 ± 0.2%, and 1.8 ± 0.2% for GEO2, GEO4, and GEO8 (Figure 9c), changes which are proportional to the ERF at the TOA. The linear regression of soil moisture change on temperature change produced negative intercept terms. Although the intercept terms were not statistically significant, they suggest that soil moisture decreased rapidly after the start of CCT, which is consistent with the rapid adjustment in global mean P − E.

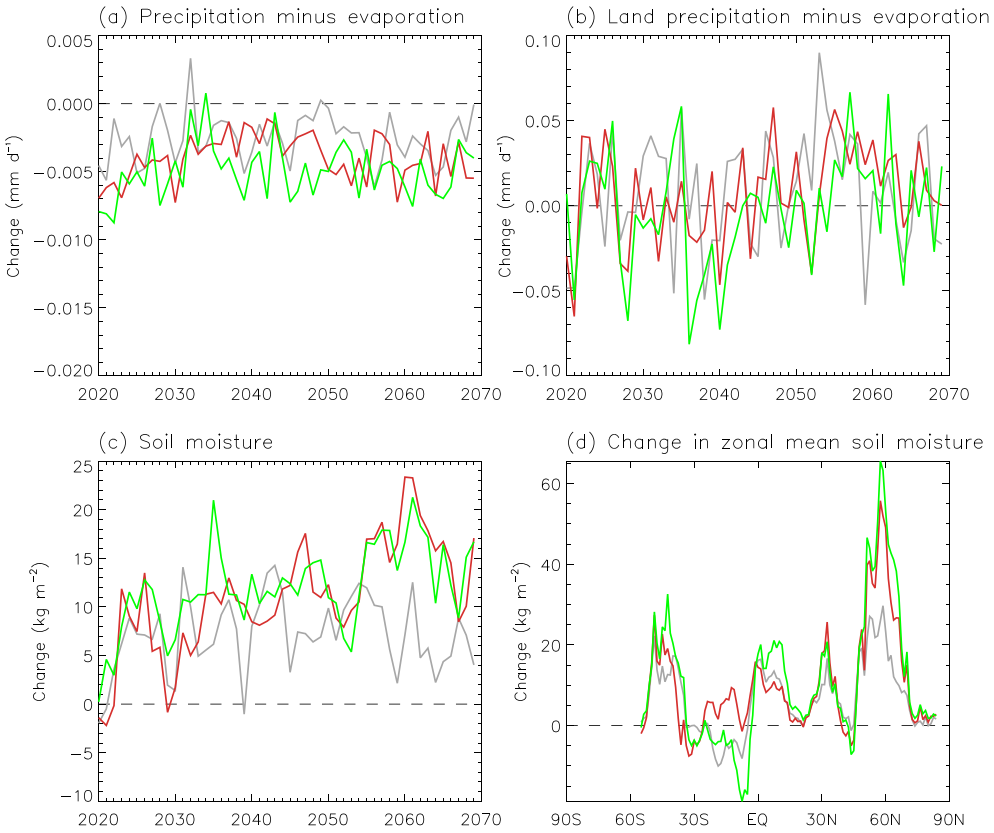

Figure 9. (a–c) Annual mean time series of differences between the three CCT simulations and RCP4.5. (d) Changes in the 2030–2069 zonal mean soil moisture for the three CCT simulations compared to RCP4.5. Color scheme: GEO2 (gray), GEO4 (brown), and GEO8 (green).

The zonal distribution of soil moisture changes was similar for the three CCT simulations (Figure 9d). The largest increases occurred in the NH middle to high latitudes and, in the tropics, in sub-Saharan Africa and southern Asia.

3.8. Physical Mechanisms for the Intensification of Precipitation and Evaporation

The increases in precipitation and evaporation following CCT occurred as rapid adjustments and were closely associated with changes in energy fluxes at the TOA and the Earth's surface that act to increase the rate of LW radiative cooling of the atmosphere (section 3.6). Increased radiative cooling was balanced by increased latent heating of the atmosphere from increased condensation of water vapor and constrained the change in precipitation [*Pendergrass and Hartmann*, 2014]. In this section we establish the relationships between changes in precipitation, vertical motion, and moisture divergence. We also identify climate and surface energy budget responses which promoted the increase in evaporation. We present results averaged over the first year of the simulation, year 2020, to investigate the rapid adjustments (fast responses) of precipitation and evaporation, an approach used by *Kravitz et al.* [2013b] in their analysis of hydrological cycle changes under geoengineering. We also show changes averaged over 2030–2069.

Enhanced radiative cooling of the large-scale atmosphere was accompanied by physical changes in the vertical motions of the atmosphere. The rate of vertical circulation in the Walker and Hadley cells intensified with CCT (Figure 10). The Walker and Hadley indices shown in Figure 10 are based on vertical pressure velocity at 500 hPa (omega500), similar to indices defined by *Wang* [2005] and *Muri et al.* [2014]. Our Walker and Hadley indices show the difference in omega500 averaged separately over grid cells of ascent and descent with positive index values representing more intense updrafts of air than subsidence. The Walker index was based on the equatorial Pacific Ocean between latitudes 5°S and 5°N and between longitudes 120°E and 100°W. The Hadley cell index was based on the region between latitudes 30°S and 30°N and between longitudes 120°E and 100°W

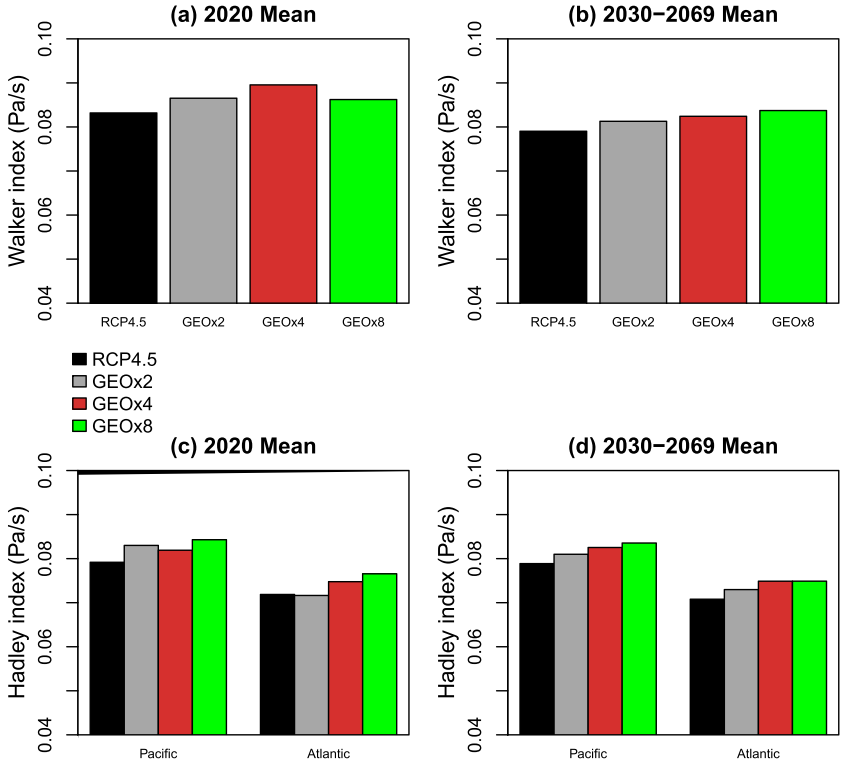

Figure 10. (a and b) Annual mean Walker index. (c and d) Annual mean Hadley cell indices for the equatorial Pacific Ocean and a region centered on the equatorial Atlantic Ocean.

(for the Pacific Ocean) and between longitudes 75°W and 15°W (for a region centered on the Atlantic Ocean). An intensification of atmospheric circulation in the tropics with CCT was also found by *Muri et al.* [2014].

Changes in omega500 were closely coupled with the changes in precipitation (Figure 11a). Precipitation increased 13% in regions of upward motion common to GEO2 and RCP4.5 during 2020. In contrast, precipitation decreased 13% in regions of downward motion. While there was a positive, approximately linear relationship between omega500 for GEO2 and RCP4.5 (Figure 11b), there were also wide variations in the distribution of changes to omega500 which would have contributed to large regional variations in precipitation response to CCT.

Changes in low-level (850 hPa) atmospheric moisture divergence were also closely associated with changes in precipitation. Precipitation in GEO2 increased 22% compared to RCP4.5 in 2020 in regions with decreased moisture divergence. In contrast, precipitation decreased 17% in regions of strengthened moisture divergence. Figure 11c shows that relatively small changes in moisture flux divergence were experienced over a large fraction of the Earth's surface, although there were some much larger regional variations. Figure 11 only shows changes for GEO2 compared to RCP4.5. Similar results were found for GEO4 and GEO8.

The surface evaporation increased for two reasons: an increase in available energy at the surface and changes in boundary layer environmental conditions that were favorable for evaporation. The increase in available surface energy was provided, in part, by increased downwelling shortwave radiation due to thinned cirrus clouds. Increased surface latent fluxes were also promoted by increased low-level wind speeds driven by the strengthened tropical circulation, increased turbulent heat fluxes in the boundary layer, and increased boundary layer height. Figures 12a and 12b show the differences for surface latent heat flux changes between regions of increase and regions of decrease in net SW radiation, sensible heat fluxes, wind speeds, and boundary layer height. Increased surface latent heat fluxes, and by inference evaporation, were associated with increases in each of these variables.

Energy available at the Earth's surface for evaporation was further promoted by a decrease in the net surface energy balance at the surface which is shown in the breakdown of the global annual mean surface energy

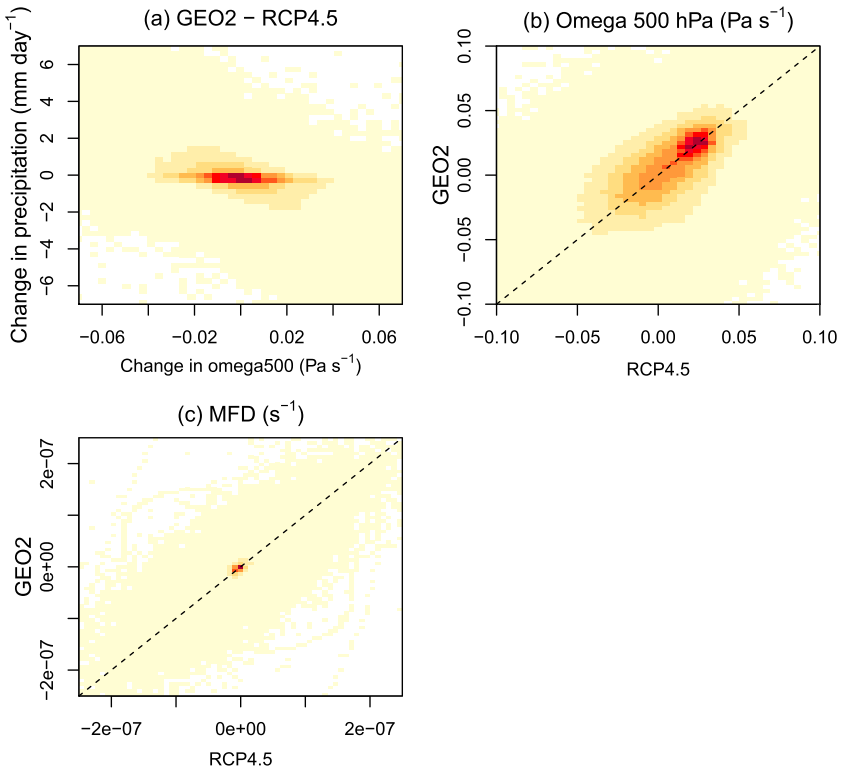

Figure 11. Surface area-weighted density distribution based on year 2020 annual mean data for (a) the change in precipitation against the change in vertical velocity at 500 hPa, (b) vertical velocity at 500 hPa for GEO2 against RCP4.5, and (c) moisture flux divergence for GEO2 against RCP4.5.

budget (Figures 12c and 12d). Positive surface energy balances under RCP4.5, which largely represent energy sequestered to subsurface ocean storage, were greatly reduced under CCT, particularly in its fast response to forcing (Figure 12c). This contributed to the strong and rapid increases in precipitation and evaporation under CCT. Moreover, it underlines the roles played by surface heat flux changes and ocean dynamics.

4. Discussion and Conclusions

We find that the combination of opposing SW and LW radiative forcings by increasing ice particle fall speed results in nonlinear forcing and climate response relationships. CCT, if it works as intended, would lead to significant changes in ice particle sizes. Although such ice particle size changes are not explicitly represented in this study, our results captured the large-scale changes in physical climate [*Storelvmo et al*., 2014], energy budgets [*Kleidon and Renner*, 2013; *Kleidon et al*., 2015], and rapid adjustment responses [*Kravitz et al*., 2013b] we expected to accompany CCT.

ERF at the TOA varied nonlinearly with the increase in fall speed; positive SW radiative forcing increased more rapidly than negative LW radiative forcing driven by greater depletion of ice particles and nonlinear changes in low/middle-level cloud with greater fall speeds. Relationships between ERF and global mean climate responses varied due to differences in driving mechanisms and time scales of response, backed up by coherent energy budget changes. Global mean temperature increased linearly with ERF at the TOA, Arctic temperature changes were amplified compared to global temperatures and were nonlinear with forcing, TCWV changes occurred as a feedback response to tropospheric temperature changes, and cloud cover and precipitation changes were linear with changes in the net radiative cooling of the atmosphere and nonlinear with ERF at the TOA. In terms of time scales, temperature changes occurred within 5–10 years of geoengineering and water vapor changes tracked tropospheric temperature changes; cloud cover decreased exclusively as a rapid adjustment; and precipitation changes involved both a rapid adjustment, which was linear with net radiative forcing of the atmosphere, and a feedback response which was linear with temperature.

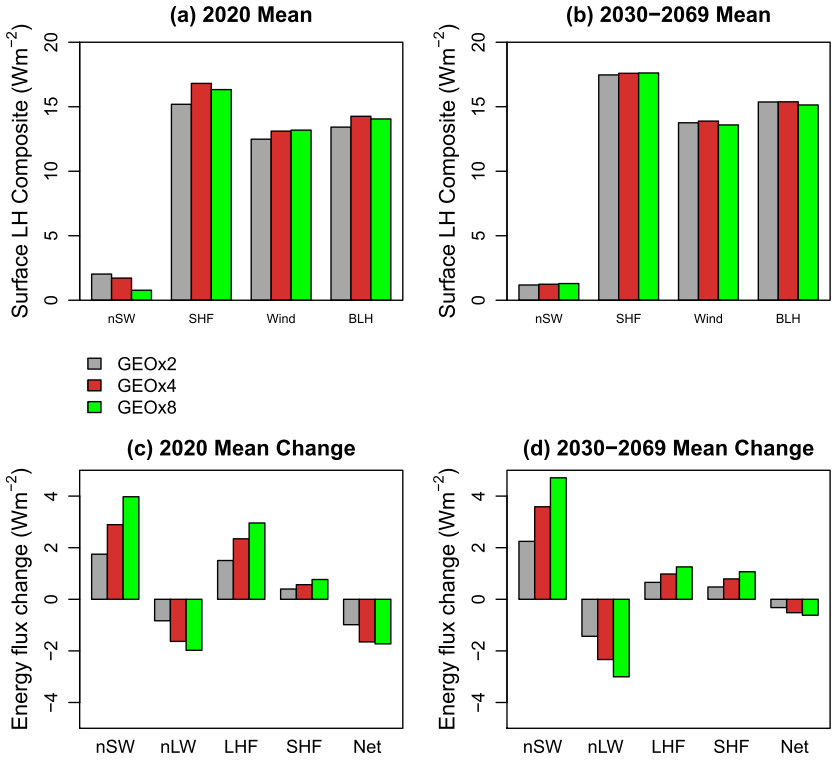

Figure 12. (a and b) A composite measure of surface latent heat flux changes. The surface latent heat composite is based on differences between annual mean surface latent heat flux changes for regions of increase and regions of decrease in net SW radiation, sensible heat flux, wind speed, and boundary layer height. A positive value for the surface latent heat composite shows that increases in latent heat flux were associated with increases in the explanatory variable (i.e., net SW radiation, sensible heat, wind speed, or boundary layer height). (c and d) Changes in the global annual mean surface energy budget terms. Positive (negative) values show the increase (decrease) in each surface energy budget term and Net = nSW + nLW-LHF-SHF.

The trade-off between opposing positive SW and negative LW radiative forcings was integrated into the seeding strategy of *Storelvmo et al.* [2014], where seeding ice nuclei concentrations were varied depending on latitude and season to minimize the occurrence of positive forcings at regional scales. An alternative approach for managing the opposing forcings would be to simulate CCT in combination with SRM methods. This would enhance the scalability of geoengineering and attenuate the SW forcing of CCT. Further, a simulation study where the amount of geoengineering is adjusted in response to emerging information on the climate state and climate response to geoengineering [e.g., *Kravitz et al.*, 2014a; *Jackson et al.*, 2015] would provide valuable insight into the benefits of combining CCT with SRM and the challenges brought by the nonlinear forcing and climate response relationships of CCT. It would also be interesting to weigh the climate change impacts on solar power generation [*Crook et al.*, 2011] against the potential benefits from increased surface SW radiation from CCT.

Increased precipitation in response to CCT was previously found by *Storelvmo and Herger* [2014] but is particularly pronounced in this study and in *Crook et al.* [2015]. *Kristjánsson et al.* [2015] also found that CCT causes intensification of the latent heat flux and precipitation and attributed it to enhanced radiative cooling of the atmosphere. By using a coupled atmosphere-ocean GCM simulation of CCT with a dynamical three-dimensional ocean, we find that intensification of precipitation and evaporation is also promoted by coherent changes in the surface energy budget and by intensification of the vertical circulations of the troposphere. Such intensification of precipitation and Hadley and Walker cell circulations in the tropics would intensify convective processes and enhance production of cirrus cloud. This negative feedback response in cirrus clouds to CCT was accounted for within our simulations. It would, however, implicitly contribute toward the cost and complexity of any real-world deployment of CCT. It would be informative for future research to quantify this effect and determine if it could be pivotal in the economic assessment of CCT compared with other geoengineering proposals.

Ensemble simulations of CCT by many more coupled atmosphere-ocean GCMs, e.g., as planned within phase 6 of the GeoMIP modeling framework [*Kravitz et al.*, 2015], would help quantify the climate model

contribution to uncertainty. Consolidated multimodel results would also facilitate investigation of the complex regional-scale changes to the hydrological cycle (precipitation, evaporation, and soil moisture changes). These have only been touched on in our results but have previously been shown to involve regional trade-offs likely to be critical in the assessment of any geoengineering strategy [e.g., *Kravitz et al*., 2014b; *Yu et al*., 2015] and to present a significant challenge for CCT as it does for SRM [*Crook et al*., 2015].

Parameterization of deep convection is a prominent source of uncertainty in simulations of large-scale climate models [*Prein et al*., 2015] that is particularly relevant to the simulation of CCT in climate models. The increases in precipitation from CCT in our results occurred mainly in tropical and neighboring subtropical regions. Our increase in fall speed was applied to ice detrained from deep convection which, in practice, would not be directly affected by CCT. The genesis of a large proportion of cirrus clouds can be traced back to the high-level outflows from deep convective cloud systems in the tropics [*Mace et al*., 2006; *Sassen et al*., 2009]. There are also uncertainties associated with the efficacy of seeding deep convective clouds in the troposphere [*Muri et al*., 2014; *Storelvmo et al*., 2014]. The uncertainty in modeling tropical convection also extends to climate feedback initiated by seeding tropical cirrus clouds and associated changes in atmospheric circulation in the tropics and in the distribution and character of tropical precipitation. This is not just an issue for our study. Further observations and fundamental research in the laboratory and in cloud-resolving models will be necessary to address the persistent uncertainties in convection and ice cloud microphysics parameterizations of GCMs highlighted by, among others, *Dionisi et al.* [2013] (uncertainties in ice crystal fall speeds), *Muhlbauer et al.* [2015] (uncertainties in upper tropospheric humidity and aerosol composition and size distribution), and *Sherwood et al.* [2014] (uncertainties in strength of convective mixing in lower and middle troposphere).

Acknowledgments

We thank all participants on the Integrated Assessment of Geoengineering Proposals project and acknowledge financial support under grant EP/I014721/1 from the Engineering and Physical Sciences Research Council (EPSRC) and the Natural Environment Research Council (NERC). P.F. was supported by a Royal Society Wolfson Merit Award, and L.S.J. was supported by the Department for International Development and the NERC (NE/M017176/1). This work made use of HECToR, the UK's national high-performance computing service, provided by UoE HPCx Ltd., at the University of Edinburgh, Cray Inc., and NAG Ltd., and funded by the Office of Science and Technology through EPSRC's High End Computing Programme. We gratefully acknowledge the reviewers for their comments and suggestions that greatly improved the quality of the manuscript. Model data are available on request from L.S.J. (l.s.jackson@leeds.ac.uk).

References

Andrews, T., P. M. Forster, O. Boucher, N. Bellouin, and A. Jones (2010), Precipitation, radiative forcing and global temperature change, *Geophys. Res. Lett.*, *37*, L14701, doi:10.1029/2010GL043991.

Bala, G., P. B. Duffy, and K. E. Taylor (2008), Impact of geoengineering schemes on the global hydrological cycle, *Proc. Natl. Acad. Sci. U.S.A.*, *105*, 7664–7669, doi:10.1073/pnas.0711648105.

Boucher, O., P. M. Forster, N. Gruber, M. Ha-Duong, M. G. Lawrence, T. M. Lenton, A. Maas, and N. E. Vaughan (2014), Rethinking climate geoengineering categorisation in the context of climate change mitigation and adaptation, *WIREs Clim. Change*, *5*, 23–35, doi:10.1002/wcc.261.

Corner, A., and N. Pidgeon (2014), Geoengineering, climate change scepticism and the "moral hazard" argument: An experimental study of UK public perceptions, *Phil. Trans. Royal Soc. A*, *372*(2031), doi:10.1098/rsta.2014.0063.

Corti, T., and T. Peter (2009), A simple model for cloud radiative forcing, *Atmos. Chem. Phys.*, *9*, 5751–5758.

Cox, P. M., R. A. Betts, C. B. Bunton, R. L. H. Essery, P. R. Rowntree, and J. Smith (1999), The impact of new land surface physics on the GCM simulation of climate and climate sensitivity, *Clim. Dyn.*, *15*, 183–203.

Crook, J., L. S. Jackson, S. M. Osprey, and P. M. Forster (2015), A comparison of temperature and precipitation responses to different Earth radiation management geoengineering schemes, *J. Geophys. Res. Atmos.*, *120*, 9352–9373, doi:10.1002/2015JD023269.

Crook, J. A., L. A. Jones, P. M. Forster, and R. Crook (2011), Climate change impacts on future photovoltaic and concentrated solar power energy output, *Energy Environ. Sci.*, *4*, 3101–3109, doi:10.1039/c1ee01495a.

Cziczo, D. J., K. D. Froyd, C. Hoose, E. J. Jensen, M. Diao, M. A. Zondlo, J. B. Smith, C. H. Twohy, and D. M. Murphy (2013), Clarifying the dominant sources and mechanisms of cirrus cloud formation, *Science*, *340*, 1320–1324, doi:10.1126/science.1234145.

Dionisi, D., P. Keckhut, C. Hoareau, N. Montoux, and F. Congeduti (2013), Cirrus crystal fall velocity estimates using the match method with ground-based lidars: First investigation through a case study, *Atmos. Meas. Tech.*, *6*, 457–470, doi:10.5194/amt-6-457-2013.

Essery, R. L. H., M. J. Best, R. A. Betts, P. M. Cox, and C. M. Taylor (2003), Explicit representation of subgrid heterogeneity in a GCM land-surface scheme, *J. Hydrometeorol.*, *4*, 530–543.

Fletcher, N. H. (1962), *Physics of Rain Clouds*, Cambridge Univ. Press, London.

Frierson, D. M. W., and Y.-T. Hwang (2011), Extratropical influence on ITCZ shifts in slab ocean simulations of global warming, *J. Clim.*, *25*, 720–733, doi:10.1175/JCLI-D-11-00116.1.

Frierson, D. M. W., Y.-T. Hwang, N. S. Fuckar, R. Seager, S. M. Kang, A. Donohoe, E. A. Maroon, X. Liu, and D. S. Battisti (2013), Contribution of ocean overturning circulation to tropical rainfall peak in the Northern Hemisphere, *Nat. Geosci.*, *6*, doi:10.1038/NGEO1987.

Gregory, J. M., and J. M. Webb (2008), Tropospheric adjustment induces a cloud component in CO_2 forcing, *J. Clim.*, *21*, 58–71, doi:10.1175/2007JCLI1834.1.

Gregory, J. M., W. J. Ingram, M. A. Palmer, G. S. Jones, P. A. Stott, R. B. Thorpe, J. A. Lowe, T. C. Johns, and K. D. Williams (2004), A new method for diagnosing radiative forcing and climate sensitivity, *Geophys. Res. Lett.*, *31*, L03205, doi:10.1029/2003GL018747.

Hardiman, S. C., N. Butchart, T. J. Hinton, S. M. Osprey, and L. J. Gray (2012), The effect of a well-resolved stratosphere on surface climate: Differences between CMIP5 simulations with high and low top versions of the Met Office climate model, *J. Clim.*, *25*(20), 7083–7099, doi:10.1175/JCLI-D-11-00579.1.

Haywood, J. M., A. Jones, N. Bellouin, and D. Stephenson (2013), Asymmetric forcing from stratospheric aerosols impacts Sahelian rainfall, *Nat. Clim. Change*, *3*, 660–665, doi:10.1038/NCLIMATE1857.

Heymsfield, A. J., and L. M. Miloshevich (1995), Relative humidity and temperature influences on cirrus formation and evolution: Observations from wave clouds and FIRE II, *J. Atmos. Sci.*, *52*(23), 4302–4326.

Hong, Y., and G. Liu (2015), The characteristics of ice cloud properties derived from CloudSat and CALIPSO measurements, *J. Clim.*, *28*, 3880–3901, doi:10.1175/JCLI-D-14-00666.1.

Jackson, L. S., J. A. Crook, A. Jarvis, D. Leedal, A. Ridgwell, N. Vaughan, and P. M. Forster (2015), Assessing the controllability of Arctic sea ice extent by sulfate aerosol geoengineering, *Geophys. Res. Lett.*, *42*, 1223–1231, doi:10.1002/2014GL062240.

Kang, S. M., I. M. Held, D. M. W. Frierson, and M. Zhao (2008), The response of the ITCZ to extratropical thermal forcing: Idealized slab-ocean experiments with a GCM, *J. Clim.*, *21*, 3521–3532.
Kleidon, A., and M. Renner (2013), A simple explanation for the sensitivity of the hydrologic cycle to surface temperature and solar radiation and its implications for global climate change, *Earth Syst. Dyn.*, *4*, 455–465, doi:10.5194/esd-4-455-2013.
Kleidon, A., B. Kravitz, and M. Renner (2015), The hydrological sensitivity to global warming and solar geoengineering derived from thermodynamic constraints, *Geophys. Res. Lett.*, *42*, 138–144, doi:10.1002/2014GL062589.
Kravitz, B., A. Robock, O. Boucher, H. Schmidt, K. E. Taylor, G. Stenchikov, and M. Schulz (2011), The Geoengineering Model Intercomparison Project (GeoMIP), *Atmos. Sci. Let.*, *12*, 162–167, doi:10.1002/asl.316.
Kravitz, B., et al. (2013a), Climate model response from the Geoengineering Model Intercomparison Project (GeoMIP), *J. Geophys. Res. Atmos.*, *118*, 8320–8332, doi:10.1002/jgrd.50646.
Kravitz, B., et al. (2013b), An energetic perspective on hydrological cycle changes in the Geoengineering Model Intercomparison Project, *J. of Geophys. Res. Atmos.*, *118*, 13,087–13,102, doi:10.1002/2013JD020502.
Kravitz, B., D. G. MacMartin, D. T. Leedal, P. J. Rasch, and A. J. Jarvis (2014a), Explicit feedback and the management of uncertainty in meeting climate objectives with solar geoengineering, *Environ. Res. Lett.*, *9*, 044006, doi:10.1088/1748-9326/9/4/044006.
Kravitz, B., et al. (2014b), A multi-model assessment of regional climate disparities caused by solar geoengineering, *Environ. Res. Lett.*, *9*, 074013, doi:10.1088/1748-9326/9/7/074013.
Kravitz, B., et al. (2015), The Geoengineering Model Intercomparison Project Phase 6 (GeoMIP6): Simulation design and preliminary results, *Geosci. Model Dev.*, *8*, 3379–3392, doi:10.5194/gmd-8-3379-2015.
Kristjánsson, J. E., H. Muri, and H. Schmidt (2015), The hydrological cycle response to cirrus cloud thinning, *Geophys. Res. Lett.*, *42*, 10,807–10,815, doi:10.1002/2015GL066795.
Mace, G. G., M. Deng, B. Soden, and E. Zipser (2006), Association of tropical cirrus in the 10–15-km layer with deep convective sources: An observational study combining millimeter radar data and satellite-derived trajectories, *J. Atmos. Sci.*, *63*, 480–503.
Martin, G. M., et al. (2011), The HadGEM2 family of Met Office Unified Model climate configurations, *Geosci. Model Dev.*, *4*, 723–757, doi:10.5194/gmd-4-723-2011.
Mauritsen, T., and B. Stevens (2015), Missing iris effect as a possible cause of muted hydrological change and high climate sensitivity in models, *Nat. Geosci.*, *8*, 346–351, doi:10.1038/NGEO2414.
Mishra, S., D. L. Mitchell, D. D. Turner, and R. P. Lawson (2014), Parameterization of ice fall speeds in midlatitude cirrus: Results from SPartICus, *J. Geophys. Res. Atmos.*, *119*, 3857–3876, doi:10.1002/2013JD020602.
Mitchell, D. L. (1996), Use of mass- and area-dimensional power laws for determining precipitation particle terminal velocities, *J. Atmos. Sci.*, *53*, 1710–1723.
Mitchell, D. L., and W. Finnegan (2009), Modification of cirrus clouds to reduce global warming, *Environ. Res. Lett.*, *4*, 045102, doi:10.1088/1748-9326/4/4/045102.
Mitchell, J., C. Wilson, and W. Cunnington (1987), On CO_2 climate sensitivity and model dependence of results, *Q. J. R. Meteorol. Soc.*, *113*, 293–322, doi:10.1256/smsqj.47516.
Moss, R. H., et al. (2010), The next generation of scenarios for climate change research and assessment, *Nature*, *463*, 747–756, doi:10.1038/nature08823.
Muhlbauer, A., T. P. Ackerman, R. P. Lawson, S. Xie, and Y. Zhang (2015), Evaluation of cloud-resolving model simulations of midlatitude cirrus with ARM and A-train observations, *J. Geophys. Res. Atmos.*, *120*, 6597–6618, doi:10.1002/2014JD022570.
Muller, C. J., and P. A. O'Gorman (2011), An energetic perspective on the regional response of precipitation to climate change, *Nat. Clim. Change*, *1*, 266–271, doi:10.1038/nclimate1169.
Muri, H., J. E. Kristjánsson, T. Storelvmo, and M. A. Pfeffer (2014), The climatic effects of modifying cirrus clouds in a climate engineering framework, *J. Geophys. Res. Atmos.*, *119*, 4174–4191, doi:10.1002/2013JD021063.
Myhre, G., et al. (2013), Anthropogenic and natural radiative forcing, in *Climate Change 2013: The Physical Science Basis. Contribution of Working Group I to the Fifth Assessment Report of the Intergovernmental Panel on Climate Change*, edited by T. F. Stocker et al., Cambridge Univ. Press, Cambridge, U. K., New York.
Niemeier, U., H. Schmidt, K. Alterskjær, and J. E. Kristjánsson (2013), Solar irradiance reduction via climate engineering: Impact of different techniques on the energy balance and the hydrological cycle, *J. Geophys. Res. Atmos.*, *118*, 11,905–11,917, doi:10.1002/2013JD020445.
O'Gorman, P. A., R. P. Allan, M. P. Byrne, and M. Previdi (2012), Energetic constraints on precipitation under climate change, *Surv. Geophys.*, *33*, 585–608, doi:10.1007/s10712-011-9159-6.
Pendergrass, A. G., and D. L. Hartmann (2014), The atmospheric energy constraint on global-mean precipitation change, *J. Clim.*, *27*, 757–768, doi:10.1175/JCLI-D-13-00163.1.
Prein, A. F., et al. (2015), A review on regional convection-permitting climate modeling: Demonstrations, prospects, and challenges, *Rev. Geophys.*, *53*, 323–361, doi:10.1002/2014RG000475.
Rogers, R. R., and M. K. Yau (1989), *A Short Course in Cloud Physics*, 3rd ed., Pergamon Press, Oxford.
Sassen, K., Z. Wang, and D. Liu (2009), Cirrus clouds and deep convection in the tropics: Insights from CALIPSO and CloudSat, *J. Geophys. Res.*, *114*, D00H06, doi:10.1029/2009JD011916.
Sherwood, S. C., S. Bony, and J.-L. Dufresne (2014), Spread in model climate sensitivity traced to atmospheric convective mixing, *Nature*, *505*, 37–42, doi:10.1038/nature12829.
Storelvmo, T., and N. Herger (2014), Cirrus cloud susceptibility to the injection of ice nuclei in the upper troposphere, *J. Geophys. Res. Atmos.*, *119*, 2375–2389, doi:10.1002/2013JD020816.
Storelvmo, T., J. E. Kristjansson, H. Muri, M. Pfeffer, D. Barahona, and A. Nenes (2013), Cirrus cloud seeding has potential to cool climate, *Geophys. Res. Lett.*, *40*, 178–182, doi:10.1029/2012GL054201.
Storelvmo, T., W. R. Boos, and N. Herger (2014), Cirrus cloud seeding: A climate engineering mechanism with reduced side effects?, *Philos. Trans. R. Soc. London, Ser. A*, *372*, 20140116, doi:10.1098/rsta.2014.0116.
Tilmes, S., et al. (2013), The hydrological impact of geoengineering in the Geoengineering Model Intercomparison Project (GeoMIP) *J, Geophys. Res. Atmos.*, *118*, 11,036–11,058, doi:10.1002/jgrd.50868.
Tilmes, S., A. Jahn, J. E. Kay, M. Holland, and J.-F. Lamarque (2014), Can regional climate engineering save the summer Arctic sea ice?, *Geophys. Res. Lett.*, *41*, 880–885, doi:10.1002/2013GL058731.
Wang, C. (2005), *The Hadley Circulation: Present, Past, and Future, ENSO, Atlantic Clim. Var. Walker Hadley Circ.*, pp. 173–202 , Kluwer Acad., Dordrecht, Netherlands.
Wilson, D. R., and S. P. Ballard (1999), A microphysically based precipitation scheme for the UK Meteorological Office Unified Model, *Q. J. R. Meteorol. Soc.*, *125*, 1607–1636, doi:10.1002/qj.49712555707.

Yoshimori, M., and A. J. Broccoli (2008), Equilibrium response of an atmosphere–mixed layer ocean model to different radiative forcing agents: Global and zonal mean response, *J. Clim.*, *21*, 4399–4423.

Yu, X., J. C. Moore, X. Cui, A. Rinke, D. Ji, B. Kravitz, and J.-H. Yoon (2015), Impacts, effectiveness and regional inequalities of the GeoMIP G1 to G4 solar radiation management scenarios, *Global Planet. Change*, *129*, 10–22, doi:10.1016/j.gloplacha2015.02.010.

Zwiers, F. W., and H. von Storch (1995), Taking serial correlation into account in tests of the mean, *J. Clim.*, *8*, 336–351.